ARCHIVES OF MECHANICS
Arch. Mech. **76** (1-2), 39–60, 2024, DOI: 10.24423/aom.4378

Precursory deformation responses in different directions to catastrophic failure of uniaxially compressed sandstones

L. CHENG [1)], S. HAO[1,2)], C. LU[3)]

[1)] *School of Civil Engineering and Mechanics, Yanshan University, Qinhuangdao, China*

[2)] *State Key Laboratory of Nonlinear Mechanics, Institute of Mechanics, Chinese Academy of Sciences, Beijing, China, e-mail: hsw@ysu.edu.cn (corresponding author)*

[3)] *School of Civil and Mechanical Engineering, Curtin University, Perth, Australia*

The precursory acceleration of deformation is widely validated as a method for predicting the failure time. Damage evolution inside rocks generally results in complex strain patterns in the vicinity of failure and various responses of deformation in different directions. However, it is still unclear what the differences and similarities are during the evolution of strain components. In this paper, we compare the evolving properties of strain components in different directions based on experiments of sandstones under uniaxial compression. It is shown that the temporal patterns of vertical strains are much more complex in spatial distributions than that of horizontal strains. The horizontal strain presents two kinds of time courses characterized by precursory accelerations in both the strain localized zone and its surrounding areas, and the evolution without accelerations in positions is far from the strain localized zone. However, the vertical strain components corresponding to loading direction present complex evolving patterns with five kinds of time courses. The final amplitudes of horizontal strains are much higher than vertical components. Horizontal strains follow the power law acceleration with the well-defined exponents, but the exponents for vertical components are more scattered. Thus, horizontal strains can be applied to predict the failure time.

Key words: deformation, time courses, precursory acceleration, power law singularity, prediction.

1. Introduction

Understanding the deformation pattern evolving to catastrophic failure in rocks is fundamentally important for describing the process to fracturing in geomedia and identifying the evolving trend to natural disasters in crust such as earthquakes, landslides, and volcanic eruptions. Crustal deformation monitoring [1, 2] and measurements of the deformation evolution of rocks tested in lab [3–6] have shown the complexity and heterogeneity of evolution in

deformation patterns are related to earthquakes, volcanic eruption, and rock failure. Monitoring the evolution of a heterogeneous deformation field of rocks is crucial to reveal the failure mechanism and recognize the route to catastrophic failure. Field monitoring such as GNSS (Global Navigation Satellite System) [7–9] and InSAR (Interferometric Synthetic Aperture Radar) [8, 10] indicates that deformation localizations occur in fault zones. In laboratory experiments, the digital image correlation technique (DIC) has been widely applied to measure the deformation field [11]. In such a technique, subsets of the deformed images are numerically correlated with the reference pixels used to determine full field surface displacements. Displacements are determined from the positional differences between the centers of the reference and target subsets [12, 13]. Strain field measurements of deformed rocks illustrate the initiation and propagation process of localized zones [3, 4, 14, 15]. After an initial deformation phase characterized by random and weak fluctuation, the localization zone nucleates where the macroscopic failure finally occurs [3, 4, 16]. Strain localization is a key mechanism of catastrophic failure in rocks and serves as a precursor of the fracture plane formation [3, 4, 17]. However, the relationship between the strain field evolution and the final macroscopic failure is still unclear.

Based on the field data and experimental results, deformation, and other response quantities such as acoustic emissions and seismicity, usually present precursory accelerations that are described by Voight's relation [18–20], that is,

$$\dot{\Omega}^{-\alpha}\ddot{\Omega} = A, \tag{1.1}$$

where Ω is a monitoring response quantity such as deformation, acoustic emission, or seismic event, α indicates the degree of acceleration, and A is a constant. The superscript dot represents the first-order derivative or the second-order derivative of Ω with respect to time t.

Equation (1.1) can be further rewritten as

$$t_{\mathrm{f}} = k^{1/\beta}(\mathrm{d}\Omega/\mathrm{d}t)^{-1/\beta} + t \tag{1.2}$$

with $k = [A(\alpha-1)]^{1/(1-\alpha)}$ and $\beta = 1/(\alpha-1)$ [21, 22]. Such a failure forecast method [21–26] has been demonstrated by retrospective prediction of failure in laboratory experiments [27–31], landslides [32–34], volcanic eruptions [18, 20, 35–37], and structural health monitoring [38]. However, it is unclear whether the different components of strains present a similar trend approaching catastrophic failure.

Heterogeneous evolution of deformation is a pervasive phenomenon in failure processes of rocks [3, 4, 14, 15, 17, 39–44]. Deformation of rocks generally undergoes an early almost homogeneous spatial distribution with weak fluctuation, then the nucleation of a localized zone, and propagation of the localized zone that finally

leads to catastrophic failure [3, 4, 45, 46]. This evolving process of localization could involve the competition and selection of several nucleated localized zones, which results in the complex deformation evolution inducing catastrophic failure. Distinguishing the spatiotemporal evolving properties of different components of strains is still a challenge although it is a fundamental requirement for improving failure prediction and understanding mechanisms of catastrophic failure.

Energy release is another key mechanism of catastrophic failure. Catastrophic failure of a localized zone is driven by deformation energy release from zones outside the localized zone [3, 4, 47–49]. This could lead to various strain spatial responses and varieties of strain components in different directions. With the deformation field getting more heterogeneous in rocks, strain patterns and their evolution become more complex. Heterogeneous damage, localization, and its propagation result in a complicated stress redistribution in rocks. The specific responses of different strain components to catastrophic failure and their differences in precursory trends are still not highlighted.

In this paper, we illustrate similarities and differences in the spatiotemporal evolution of strain components in the two perpendicular directions of surface strains through DIC measurements of surface deformations in deformed sandstones under uniaxial compression, with special focus on comparing the evolving trends of strain components approaching to the catastrophic failure time.

2. Test materials and experimental methods

2.1. Test materials

The test material used in this study is yellow sandstone from Beijing, China, with a grain size of about 10 μm (Fig. 1a). These sandstones were cut into prismatic samples with a height of 40 mm and a cross-section of $16 \times 18\,\mathrm{mm}^2$ (Fig. 1b) using the GCTS RLS-100 model (Fig. 3a) rock auto-cutter. The error of unevenness of the upper and lower ends of a specimen was controlled to be within 0.03 mm, and the error along the height, length and width of the specimen was less than 0.3 mm, with the maximum deviation of the end faces not exceeding 0.25°. To determine the compressive strength and wave velocity of this type of rock, the sample was placed between two parallel indenters of the testing machine and pressure gradually increased. The maximum stress at failure, determined by the recorded force-displacement curve, is defined as the compressive strength (Fig. 2). The KON-DZY model (Kangkerui, Beijng, CN) was used in the non-metallic ultrasonic measurement on an average wave speed (Fig. 3b). During the test, we first applied petroleum jelly on both sides of a rock sample to improve the transmission efficiency of ultrasonic waves, and then placed ultrasonic probes on both sides of the sample. By recording the time for ultra-

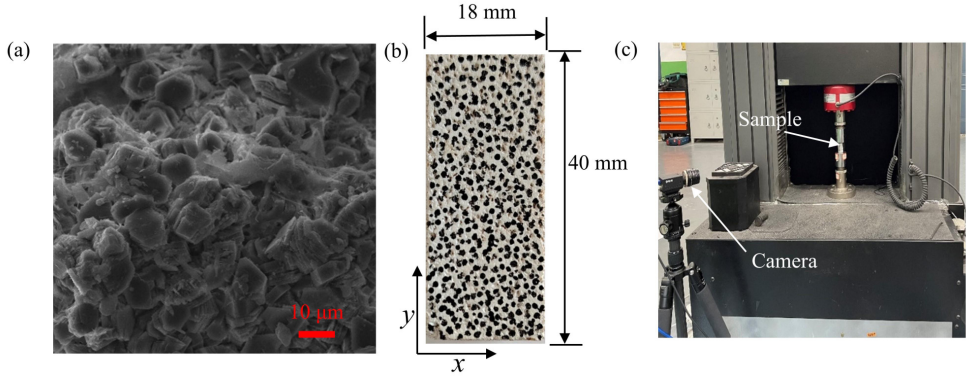

Fig. 1. Images of a sample and the experimental setup, with (a) scanning electron microscope photos under the magnification of $5000^{\times}$, (b) the artificial speckle pattern on the surface of sandstone, and (c) the experimental setup.

sonic waves travelling from one probe to the other and the distance between the two probes, the wave velocity was calculated. Here the average wave velocity is the mean value obtained by repeating this process at different locations of the sample. The indoor test physical-mechanical parameters, i.e., the average compressive strength and wave velocity, were 69.03 ± 5.61 MPa and 2.99 ± 0.09 km/s, respectively.

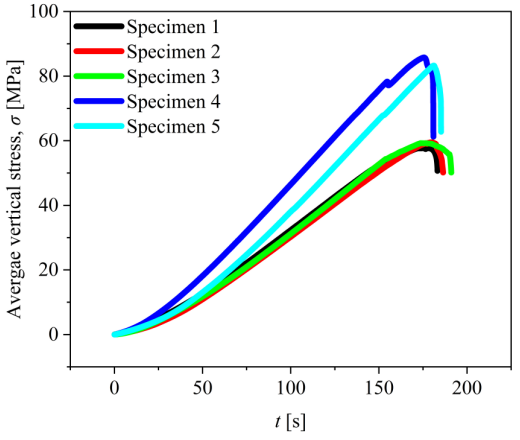

Fig. 2. The typical force versus time curves for five rock samples.

2.2. Loading methods and measuring devices

As shown in Fig. 1, for uniaxial compression experiments, the Instron 5982 model (Fig. 1c) universal testing machine (Instron, Norwood, MA, USA) was used, with a maximum load of 100 kN and the accuracy of a mechanical trans-

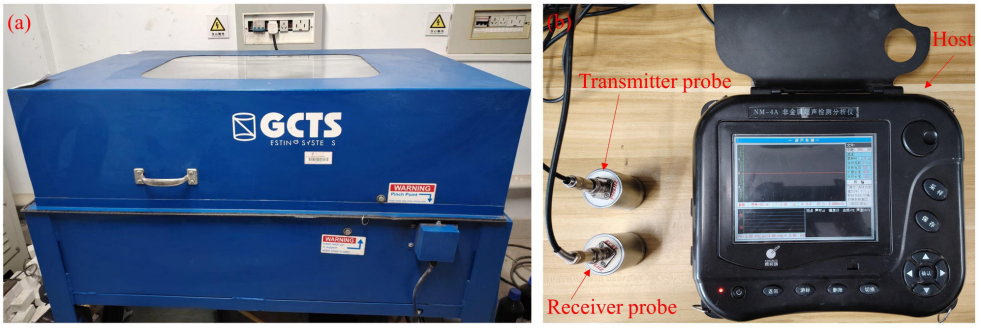

FIG. 3. Equipment for cutting rocks and detecting the wave velocity, with (a) the automatic stone cutting machine, and (b) the non-metallic ultrasonic detection analyzer.

ducer was 0.0001 N. The experiment was loaded through displacement control. Considering that the surface of a specimen cannot be flat, we firstly loaded the specimen slowly at a speed of 0.1 mm/min to avoid the eccentric compression and stress concentration due to uneven contact between the indenter and the upper surface of the specimen. Loading stopped when it reached 3 kN, and the sample was unloaded after being held for six minutes. This process repeated for three times. Then, the crosshead of the tester continued to move at a constant speed of 0.1 mm/min (Fig. 1c) to uniaxially compress the sandstone sample along the height direction until macroscopic failure. Figure 4 illustrates the failure photographs overlaid with contour plots.

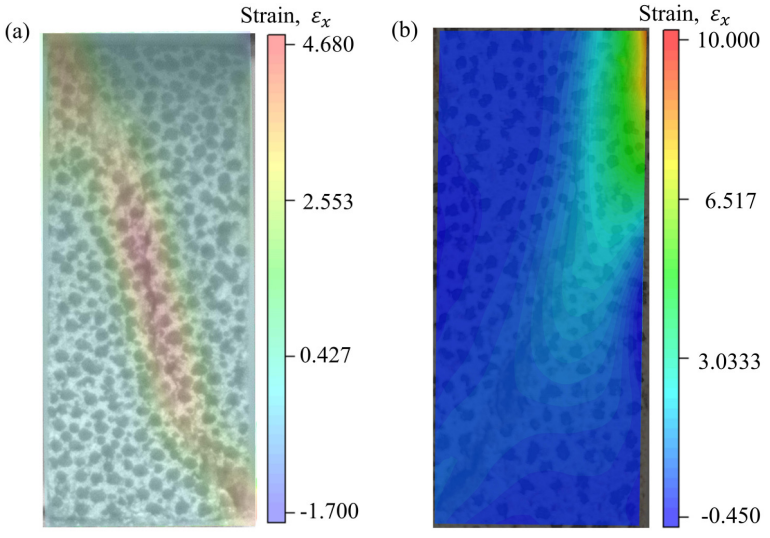

FIG. 4. The strain field just before failure for (a) specimen 1 and (b) specimen 2, where the strain field is superimposed on the failure photo of a tested specimen.

Artificial speckle patterns were applied on the surface of sandstone specimens by spraying with white matte paint. The images were captured at a frequency of 30 Hz with a 2048×2048 pixel camera positioned in front of the surface of a specimen, and DIC was used to match the subsets of two captured images with speckle patterns. The subsets of deformed images were numerically correlated with the reference subset to determine the full-field surface displacements using the correlation software PMLAB (Fig. 1c) developed by the University of Science and Technology of China (Hefei, China). The subset and step size are two key parameters in the correlation analysis. The subset size was adopted as an image window tracked by the correlation algorithm in terms of motion and deformation. The solution provides displacement components at the center of each subset. The step size is the distance between the centers of two nearest subsets. In these studies, the subset and step sizes were 29 and 4 pixels, respectively. The displacement fields were determined by the positional differences between the centers of the reference and target subsets.

3. Comparison of time courses of ε_x, ε_y and ε_{xy} evolving to failure

Five samples were tested, but for simplicity, only the results of two samples were chosen and discussed in detail. Figure 4 shows the localized region coinciding with the specimen failure contour. Under uniaxial compression of sandstones, deformation localization and its propagation dominate the failure process. Deformation processes were characterized by compaction in the vertical (y) compression direction and expansion in the horizontal (x) direction. According to strain spatial distributions and localization propagation illustrated by contours of strains ε_x, ε_y, and ε_{xy}, four marked and numbered representative locations (see inserts in Figs. 5 and 6) were selected to illustrate differences and similarities of their responses.

3.1. Time courses of horizontal components (ε_x) of strains characterized by two stages

Figures 5a and 6a plot the time courses of horizontal components (ε_x) of strains at four typical positions. Horizontal deformations are dominated by tension strains and the amplitudes of ε_x decrease with distances from the localized zone. Positions (e.g., position 1 in Figs. 5a and 6a) far from the localized zone deform slowly with low strains. With distances closing to the localized zone, horizontal components, ε_x, of strains increase and present obvious accelerating trends with approaching the failure time (e.g., positions 2 and 3 in Figs. 5a and 6a). At these positions, horizontal components, ε_x, of strains show two typical stages characterized by an early slow evolving stage with small and random fluctuation and a final accelerating stage in the vicinity of failure time.

3.2. Spatial distributions of time courses of vertical components (ε_y) of strains

Time courses (Figs. 5b and 6b) of vertical components (ε_y) of strain show much more complex patterns in spatial distributions. Vertical components (ε_y) of strains are characterized by compactions owing to the uniaxial compression load along this direction. Figures 5b and 6b show a more complex pattern of ε_y in

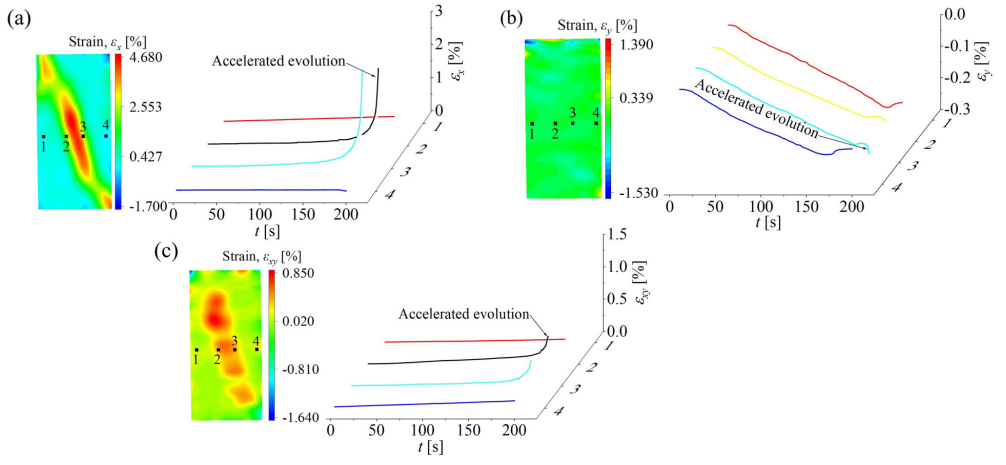

FIG. 5. Spatial distributions of typical time courses of (a) ε_x, (b) ε_y and (c) ε_{xy} in specimen 1, where the numbered dots denote positions at the calculated time courses of strains.

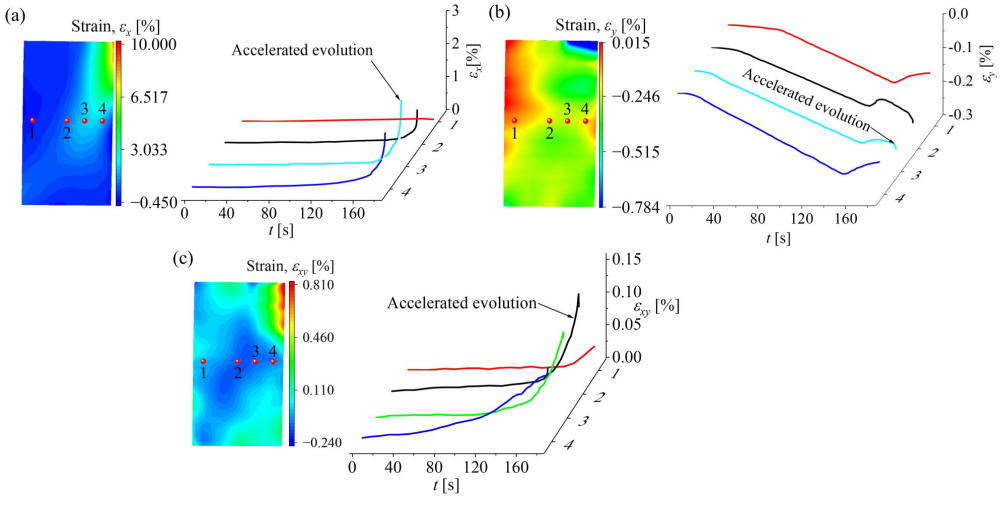

FIG. 6. Spatial distributions of typical time courses of (a) ε_x, (b) ε_y and (c) ε_{xy} in specimen 2, where the numbered dots denote positions where the calculated time courses of strains.

spatial distributions. Strain components, ε_y, in some positions (e.g., positions 1 and 4 in Figs. 5b and 6b) characterized by the decrease of strain indicate the recovery of strains in y-direction. The strain ε_y of some positions (e.g., positions 2 and 3 in Figs. 5b and 6b) transits from deceleration to acceleration in the vicinity of failure. To illustrate the evolution in detail, the contour maps of different moments of position 2 in specimen 2 were selected and analyzed (see Fig. 7), which shows the recovery of strain to the continuation of loading.

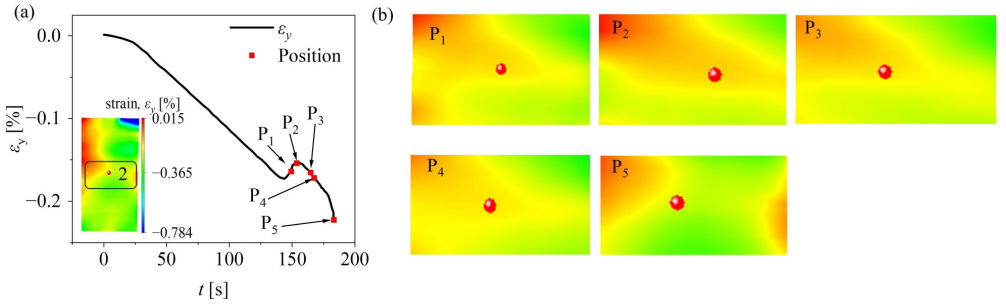

Fig. 7. The variation of ε_y along the vertical direction at position 2 in specimen 2, and the corresponding contour plots at five typical moments. (a) The change of ε_y along the vertical direction at position 2, with inset the last failure contour photograph. (b) The evolutionary contour plots for five typical moments (the enlarged area in the black box in the contour plot of inset in (a)).

3.3. Time courses of shear strains (ε_{xy}) characterized by two stages

Figures 5c and 6c plot time courses of shear strains (ε_{xy}) at four typical positions. At these positions, ε_{xy} shows almost a similar evolving trend to the horizontal strain component of ε_x. Here it is worth noting that, in contrast to ε_x, shear strains ε_{xy} at the position 1 in Figs. 5c and 6c also exhibit the precursory acceleration approaching the failure time. At all positions, shear strains, ε_{xy}, show two typical stages characterized by an early slow evolving stage with small and random fluctuation and a final accelerating stage in the vicinity of the failure time.

3.4. Response differences in ε_x, ε_y and ε_{xy} at the same locations

Five different pairs of time histories in ε_x, ε_y and ε_{xy} at the same positions were observed in experiments. To clarify the similarities and differences of strain responses in various directions at a given position, Figs. 8 and 9 illustrate the typical evolution of ε_x, ε_y and ε_{xy} in five typical individual positions. It indicates that ε_{xy} shows almost a similar trend to ε_x at any individual position. Thus, the following discussion is mainly focused on the comparison between ε_x and ε_y. However, it should be noted that final amplitudes of ε_x are much higher

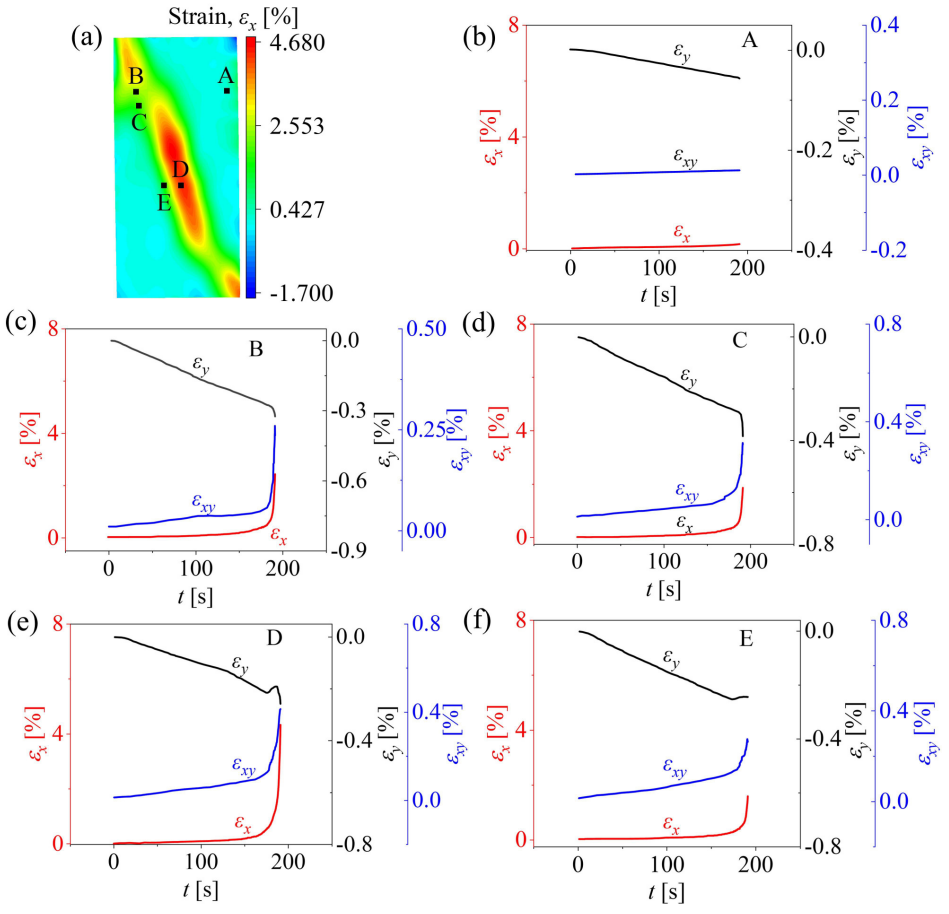

FIG. 8. (a) The strain field in specimen 1 and the corresponding time courses of ε_x, ε_y and ε_{xy} at labelled (b) A, (c) B, (d) C, (e) D, and (f) E points in (a).

than that of ε_y and ε_{xy}. Here, inflation responses of tested sandstones are much clearer and more susceptible than compactions. Time courses of ε_x are characterized by two stages of earlier linear and accelerating stages (as seen in Figs. 8 and 9c–f) or only a linear process without acceleration (as observed in Figs. 8b and 9b).

In contrast, the spatial distributions of time histories of ε_y are much complex with strain localization and its propagation. As shown in Figs. 8c, 8d, 9c and 9d, ε_y at positions B and C where the high strain zone nucleates shows the evolution with three stages: initial acceleration, linear, and final acceleration. At the position D to which the high strain zone later extends, the time course of ε_y presents four stages (Figs. 8e and 9e): initial acceleration, linear increasing, decreasing, and finally transition to acceleration till failure. The strain ε_y at the

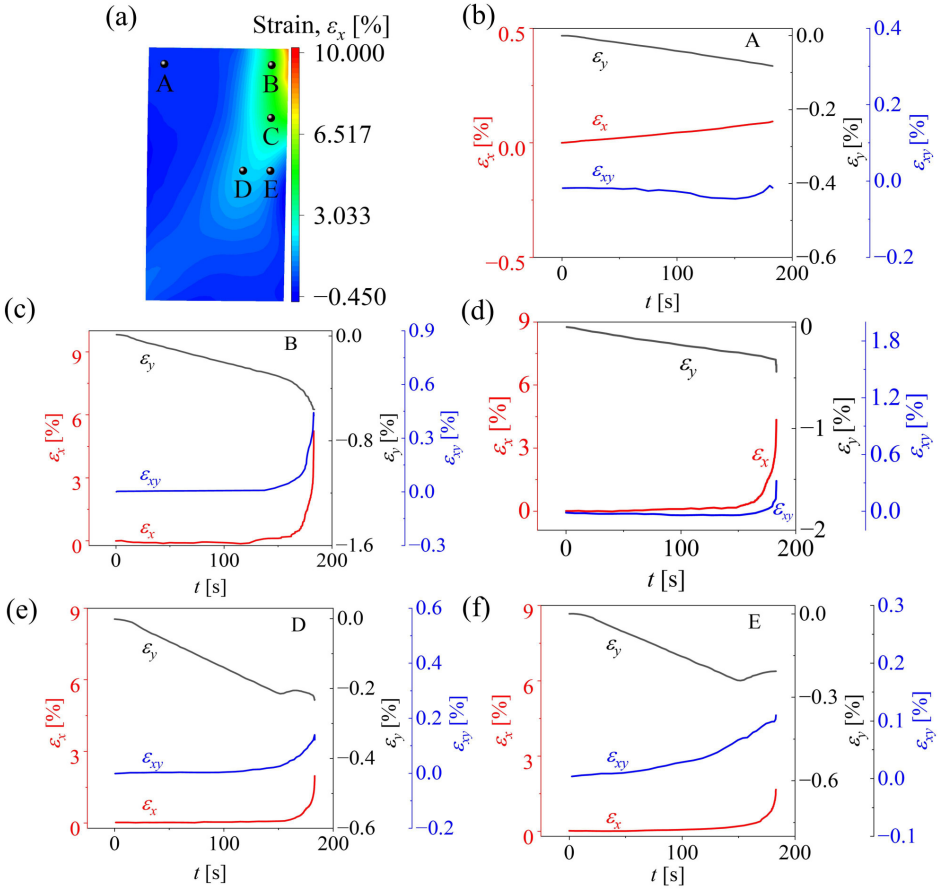

FIG. 9. (a) The strain field in specimen 2 and the corresponding time courses of ε_x, ε_y and ε_{xy} at labelled (b) A, (c) B, (d) C, (e) D, and (f) E points in (a).

position A that is far from the final strain localized zone always shows a linear and slow evolving trend (Figs. 8b and 9b). For positions (e.g., the position E in Figs. 8f and 9f) near the strain localized zone, the strain component ε_y in the y-direction decreases following the linear stage. Therefore, the position transits to releasing the stored strain energy before failure.

It is seen that the horizontal strain exhibits the regular evolution approaching failure, which is characterized by strain accelerating to failure in the strain localized zone and its surrounding areas. In the region far from a strain localized zone, strain evolves slowly without acceleration. However, the vertical strain component corresponding to the loading direction presents a complex evolving pattern in spatial distributions. The strain ε_y in areas nearby the localized zone presents strain recovering, but ε_x does not show an unloading process.

4. Precursory power law acceleration of ε_x and ε_y and the failure time prediction

4.1. Precursory power law acceleration behaviors of ε_x and ε_y

It is widely validated [18–20, 30, 34, 50–52] that the precursory acceleration of responses, such as deformation [50, 52], and acoustic emission [30], can be described as a power law relationship with respect to the failure time [18–20]. Figures 10, 11, 12 and 13 plot the double logarithmic relationships of strains of ε_x and ε_y versus the time to failure at typical positions for four samples with different peak forces and failure times. Linear parts in the vicinity of the failure time indicate the power law relationship works well in all these positions.

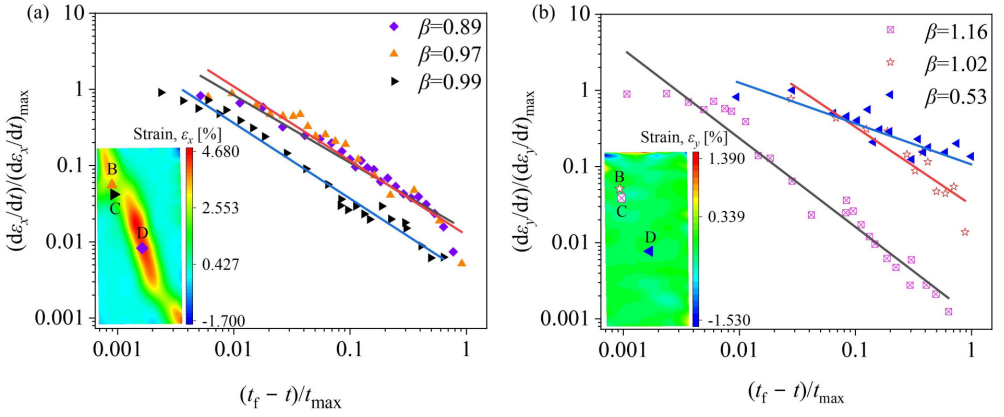

FIG. 10. The double logarithmic curves of the strain rate versus $(t_f - t)$ in specimen 1, with the precursory power law behaviours and exponents for (a) ε_x and (b) ε_y.

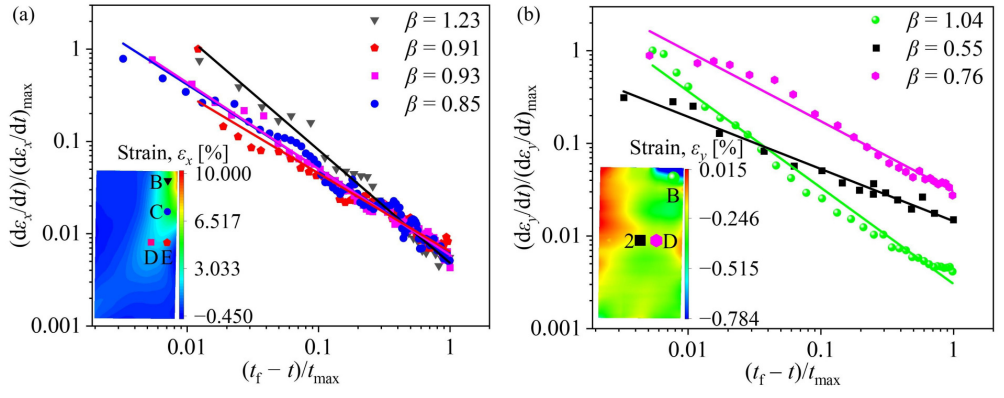

FIG. 11. The double logarithmic curves of the strain rate versus $(t_f - t)$ in specimen 2, with the precursory power law behaviours and exponents for (a) ε_x and (b) ε_y.

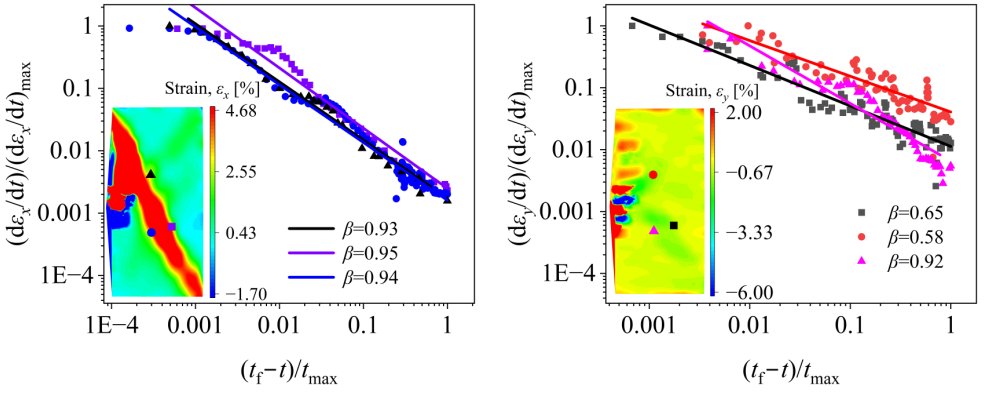

FIG. 12. The double logarithmic curves of the strain rate versus $(t_f - t)$ in specimen 4, with the precursory power law behaviours and exponents for (a) ε_x and (b) ε_y.

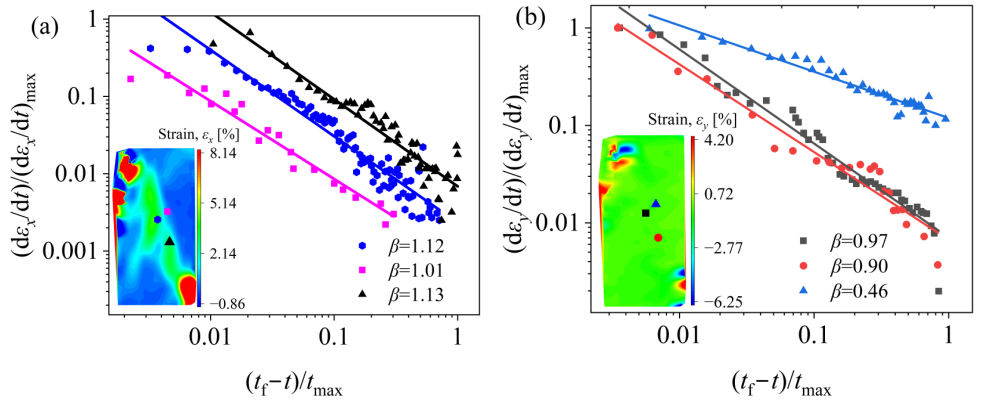

FIG. 13. The double logarithmic curves of the strain rate versus $(t_f - t)$ in specimen 5, with the precursory power law behaviours and exponents for (a) ε_x and (b) ε_y.

The least-square fitting method was used to fit the critical power law exponent. The data points used for fitting were determined according to the principle of the maximum correlation coefficient [30, 52]. Values of the critical exponents, β, of accelerations of ε_x show smaller scatters than ε_y.

4.2. Failure time prediction

To validate different responses at the same position, retrospective predictions were performed based on a rewritten form of Eq. (1.2), that is,

$$(\mathrm{d}\varepsilon/\mathrm{d}t)^{-1/\beta} = k^{-1/\beta}(t_\mathrm{f} - t). \tag{4.1}$$

A "cumulative time technique" [22] was applied to perform prediction. Each fitting starts from the same fixed time in the precursory acceleration phase but

ends at every individual time. Consequently, the number of data points used for fitting increases with time as it approaches the failure time. The failure time is assumed to be unknown and only the data preceding an individual time were

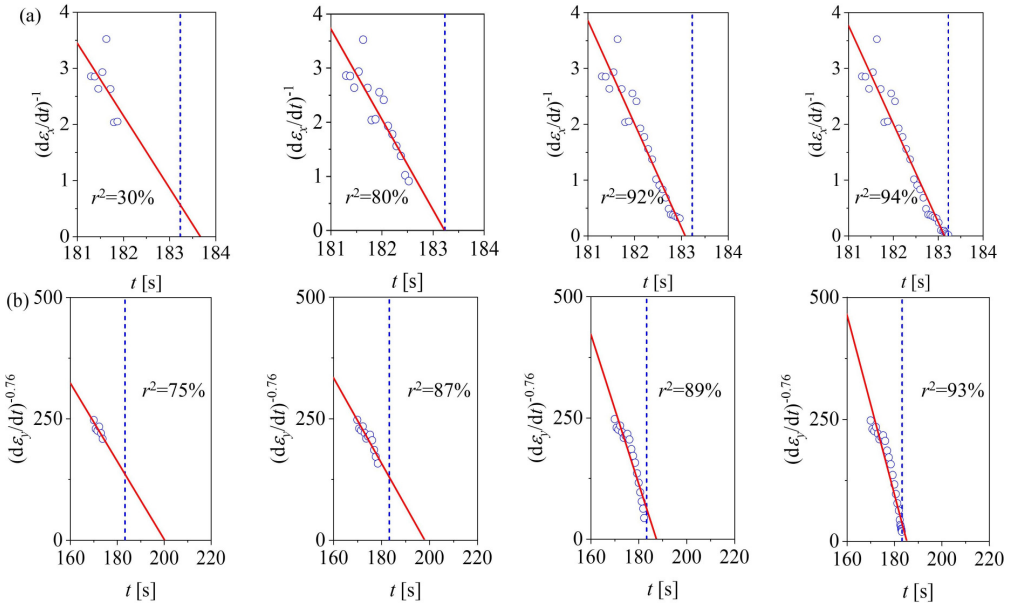

FIG. 14. The predicting process and predicted results in specimen 2 for (a) the horizontal strain rates and (b) the vertical strain rates, where scattered cycles are experimental data. The solid lines indicate the fitted results and the intersection point with the time axis is the predicted results.

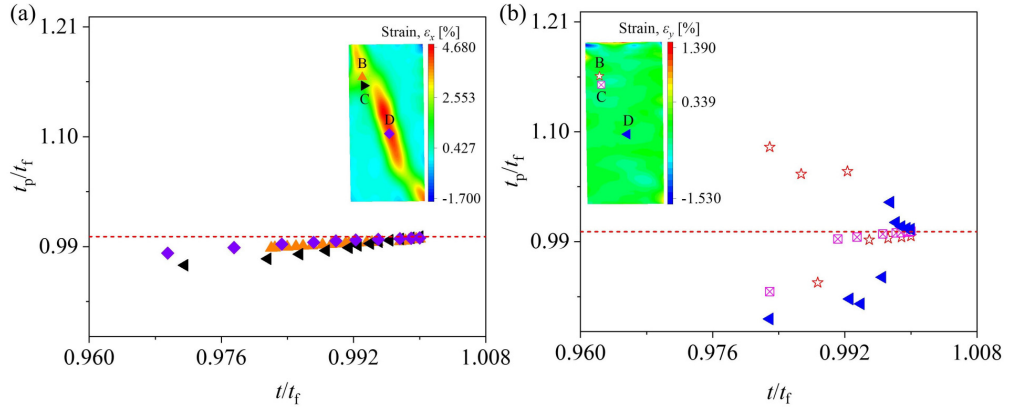

FIG. 15. The predicted results approaching to the catastrophic failure time based on (a) the horizontal and (b) vertical strain rates in specimen 1, respectively. The inset shows four representative positions where strain rates are used for prediction.

chosen in the projection – all "future" data were ignored – allowing the true prediction to be made. A linear least-squares method was adopted to obtain the best fit linear trend. The trend is then extrapolated to determine the predicted failure time. To demonstrate the prediction process, the analytical results from specimen 2 are given, with the fitted linear correlation coefficient r^2 being used to evaluate the linear regression model. The intersection of the red fitting line with the time axis is the predicted results. As seen in Fig. 14, the linear correlation coefficients become larger and larger as the number of data points increases. This suggests that as the number of data points increases, the trend of the data

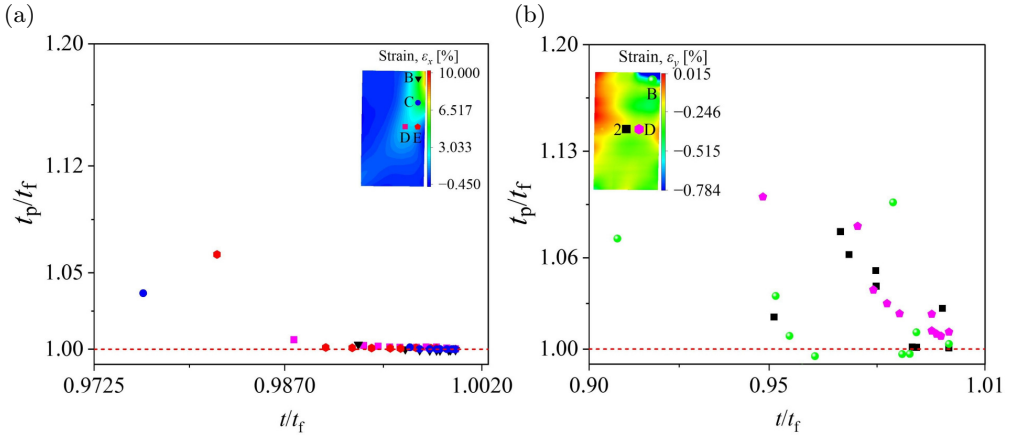

Fig. 16. The predicted results approaching to the catastrophic failure time based on (a) the horizontal and (b) vertical strain rates in specimen 2, respectively. The inset shows four representative positions where strain rates are used for prediction.

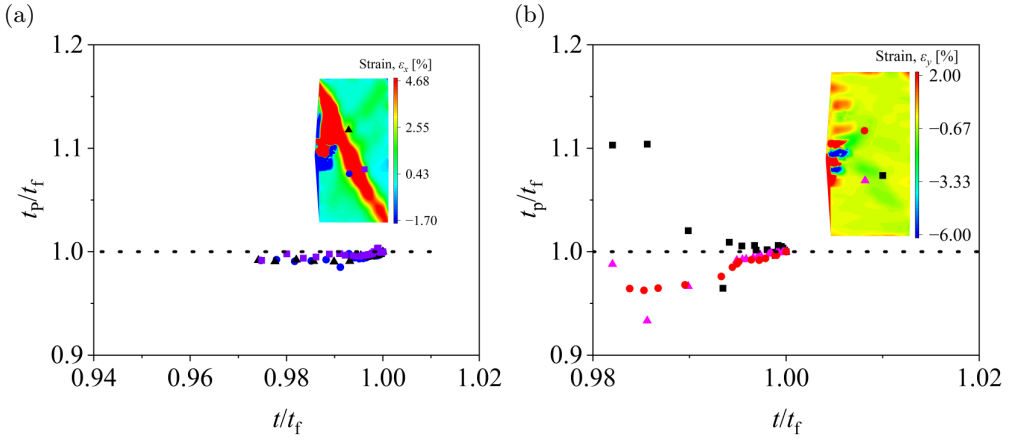

Fig. 17. The predicted results approaching to the catastrophic failure time based on (a) the horizontal and (b) vertical strain rates in specimen 4, respectively. The inset shows three representative positions where strain rates are used for prediction.

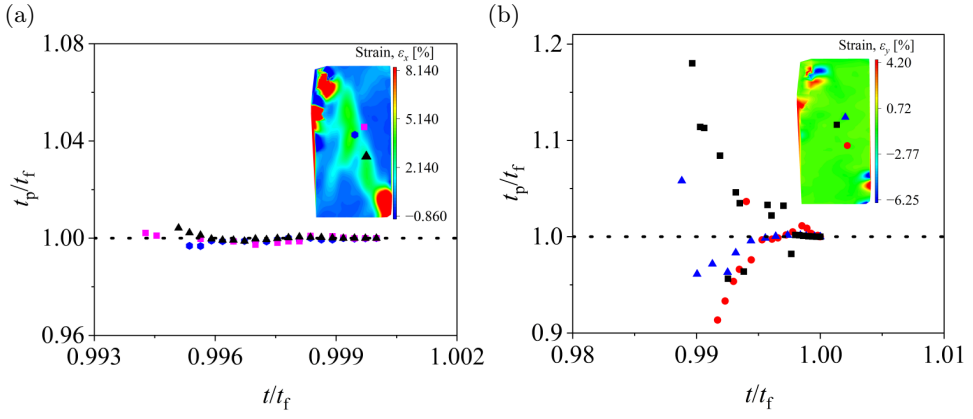

FIG. 18. The predicted results approaching the catastrophic failure time based on (a) the horizontal and (b) vertical strain rates in specimen 5, respectively. The inset shows three representative positions where strain rates are used for prediction.

evolution becomes more consistent with the linear model. The closer prediction result is the actual failure time. Figures 15, 16, 17 and 18 show the predicted results with the sampling time approaching failure. It is obvious that the predicted results of both ε_x and ε_y at these positions consistently converge to the actual value with the time closing to failure, however. the rates of ε_x give the better prediction than ε_y.

5. Discussion

5.1. Complex temporospatial patterns of deformations in the vicinity of failure time

Many methods such as GNSS [7, 53, 54] and SAR [55, 56] techniques have been developed to monitor surface deformations. Recognizing the relationship between the deformation field evolution and failure is fundamental for its prediction and understanding of the failure mechanism [3]. For the rock mass where numerous pre-existing flaws exist, advanced numerical simulations should be performed to locate and trace the plastic zone and the internal crack growth path, which can provide a useful guidance for the monitoring positions [57]. Our results declare that deformations of rock present complex evolution patterns in the vicinity of the catastrophic failure. Some positions show the decrease of strains as approaching the failure time, the others present two transitions where strain first transits from acceleration to deceleration and finally returns to acceleration. However, there are still some positions far from the localized zone, with no obvious changes in response to failure. These properties challenge the task of identifying the precursory acceleration based on monitoring the spatial deforma-

tions. This also suggests that selections of monitoring positions are crucial for identifying the precursory responses to catastrophic failure like earthquakes and landslides.

Localization is a key precursor of rock failures [3, 15, 17, 42, 43], which results in uncertainty [3, 4]. Evolution of localization can be characterized by occurrence and propagation of high strain zones. Our results show that different strain components have different spatial evolving patterns. This implies that sizes and distributions of strain localized zones are different for various strain components.

5.2. The preferable response quantity for failure prediction

A central problem for failure prediction is to find a reliable precursory signal [58–60]. The complex deformation pattern and its evolution induced by the heterogeneity of rocks result in uncertainty of precursory signals. Our results highlight the different spatial distribution properties of strain components in various directions in response to catastrophic failure. For tested sandstones, strain components, ε_y, at the compression load direction involved a combination pattern of load in the localized zone characterized by the increases of ε_y and unload behaviors in some positions close to the localized zone characterized by the decrease of ε_y, in response to failure propagation and localization evolution. In contrast, the expansion strains do not show any unload response. These findings give insights to recognize the strain field evolution in response to failure propagation and suggest clues to distinguish a precursory process of deformations for failure prediction based on monitoring surface deformations.

In the present experiments of sandstones, expansion strains and rates show much higher amplitudes than compressive and shear strains. This is also seen

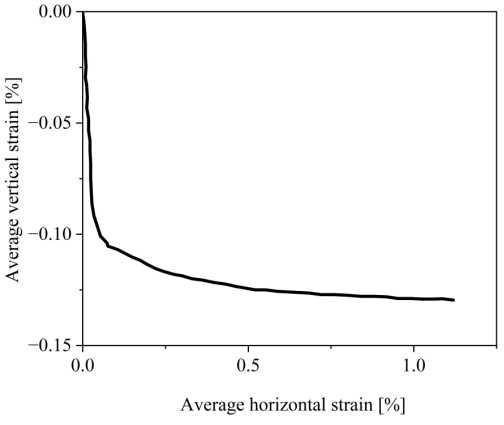

Fig. 19. The evolution of average vertical strains versus horizontal strains. The linear part in the early phase gives an estimation of Poisson's ratio of the tested sandstone as ∼0.30.

from the evolution of average vertical strains versus horizontal strains, as shown in Fig. 19. Based on the linear part in Fig. 19, Poisson's ratio of the tested sandstone can be estimated as ∼0.30. This is important to distinguish or recognize the precursory signals from normal background signals [58, 59] during field monitoring. The uncertainty of singularity exponents causes difficulty in predicting the failure time [22, 52] based on the precursory power law acceleration behaviors. Our results show that the precursory power law acceleration of horizontal strain rates presents a more consistent value of exponents than the vertical strain rates. Also, prediction based on precursory acceleration trends of horizontal strain gives a better warning to failure than the vertical strain. These results imply that expansion rates, are a preferable response quantity for failure prediction in comparison with the compression rates for sandstones.

5.3. Heterogeneities and precursory power law singularity

The catastrophic failure of brittle rocks involves nucleation, propagation, interaction, and coalescence of micro-cracks in different scales, characterized by a nonlinear evolving process of response quantities. Differences of existing microfaults and structures inside rock bodies result in differences of failure processes from sample to sample and sample-specific properties of nonlinear evolution of forces and deformations. As shown in Fig. 2, the force curves of these tested samples made by the same kind of sandstone, their peak forces, and failure times exhibit obvious heterogeneities because of differences in time series of microcracking events (much smaller than the macroscopic failure event) appearing in the failure process of different samples. It should be noted that, however, the coalescence of heterogeneously distributed micro-cracks in rock samples induces a nonlinear acceleration process of response quantities approaching the catastrophic time, which serves as a warning signal for the impending catastrophic event and is helpful for predicting the failure time. Our results show that the precursory acceleration trend of approaching the catastrophic time presents a common power law relationship with respect to the time-to-failure (Figs. 10–13), but the power law exponents β of these samples do not share a consistent value. It has been demonstrated that the common power law singularity of response rates in the proximity of the catastrophic time is governed by the energy criterion of catastrophic failure, which can be interpreted with a power function approximation [50, 52]. The variation of the power law exponent β represents different-order contacts to a catastrophic rupture process without an external work input [52], determined by the degree of a local stress controlling the damage evolution [61].

6. Conclusions

In present uniaxial compression tests on sandstones, strain components in vertical (compression direction) and horizontal directions, as well as shear strains, show different time course patterns. The final amplitudes of horizontal strains are much higher than that at the vertical direction and shear strains. Thus, inflation responses of tested sandstones are clearer and more susceptible than compressive and shear strains. Horizontal strain of surface deformations shows two typical kinds of time courses with evolving to the failure time: (1) the obvious precursory acceleration following the early linear evolution in and nearby the localized zone, and (2) the linear and slow evolution without an accelerating process in positions far from the localized zone. In contrast, vertical strain components exhibit much more complex evolution patterns with five kinds of time courses. The vertical strain components in some positions decrease, manifesting the recovery of strains, however, such a kind of response is not observed in the horizontal strain.

Even at the same position, horizontal and vertical strain components, as well as shear strains, show different responses with approaching the failure time. In the vicinity of failure, vertical strain components at some positions transit from acceleration to deceleration or decrease rapidly, but the horizontal strain component and shear strains present a monotonic acceleration.

For precursory power law accelerations, horizontal strain shows consistent power law exponents at different spatial positions than vertical components. Retrospective predictions imply that the horizontal strain rates present a better warning for the failure time.

Acknowledgements

This work is supported by the Key Research and Development Projects of Hebei Province (22375407D), the Hebei Natural Science Foundation (Grant No. D2020203001), and the National Natural Science Foundation of China (Grant No. 11672258).

Conflict of interest

The authors declare there are not any scientific or financial conflicts of interest in this work.

References

1. E. Russo, A. Tibaldi, G.P. Waite, F.L. Bonali, F. Massin, J. Farrell, *Unraveling the complex deformation pattern at yellowstone plateau through seismicity and fracture analysis*, Tectonophysics, **778**, 2020.

2. R. SPARKS, *Forecasting volcanic eruptions*, Earth and Planetary Science Letters, **210**, 1-2, 1–15, 2003.

3. S.W. HAO, H.Y. WANG, M.F. XIA, F.J. KE, Y.L. BAI, *Relationship between strain localization and catastrophic rupture*, Theoretical and Applied Fracture Mechanics, **48**, 1, 41–49, 2007.

4. S.W. HAO, M.F. XIA, F.J. KE, Y.L. BAI, *Evolution of localized damage zone in heterogeneous media*, International Journal of Damage Mechanics, **19**, 7, 787–804, 2010.

5. D. SHIROLE, G. WALTON, A. HEDAYAT, *Experimental investigation of multi-scale strain-field heterogeneity in rocks*, International Journal of Rock Mechanics and Mining Sciences, **127**, 104212, 2020.

6. J. XUE, S. W. HAO, R. YANG, P. WANG, Y.L. BAI, *Localization of deformation and its effects on power-law singularity preceding catastrophic rupture in rocks*, International Journal of Damage Mechanics, **29**, 1, 86–102, 2020.

7. V. DURAND, A. GUALANDI, S. ERGINTAV, G. KWIATEK, M. HAGHSHENAS, M. MOTAGH, G. DRESEN, P. MARTÍNEZ-GARZÓN, *Deciphering aseismic deformation along submarine fault branches below the eastern sea of Marmara (Turkey): Insights from seismicity, strainmeter, and GNSS data*, Earth and Planetary Science Letters, **594**, 117702, 2022.

8. M.Z. LYU, K.J. CHEN, C.H. XUE, N. ZANG, W. ZHANG, G.G. WEI, *Overall subshear but locally supershear rupture of the 2021 M_w7.4 Maduo earthquake from high-rate GNSS waveforms and three-dimensional InSAR deformation*, Tectonophysics, **839**, 229542, 2022.

9. J.R. MURRAY, N. BARTLOW, Y. BOCK, B. A. BROOKS, J. FOSTER, J. FREYMUELLER, W.C. HAMMOND, K. HODGKINSON, I. JOHANSON, A. LÓPEZ-VENEGAS, D. MANN, G.S. MATTIOLI, T. MELBOURNE, D. MENCIN, E. MONTGOMERY-BROWN, M.H. MURRAY, R. SMALLEY, V. THOMAS, *Regional global navigation satellite system networks for crustal deformation monitoring*, Seismological Research Letters, **91**, 2A, 552–572, 2019.

10. Y. LIU, S. HAN, L.Y. XIONG, Y.M. WEN, H.H. LI, C.J. XU, *Three-dimensional deformation velocity field and kinematic characteristic of the middle and east parts of Haiyuan fault zone from InSAR and GPS observations*, Advances in Space Research, **71**, 8, 3175–3185, 2023.

11. R. JANELIUKSTIS, X. CHEN, *Review of digital image correlation application to large-scale composite structure testing*, Composite Structures, **271**, 114143, 2021.

12. B. PAN, *Digital image correlation for surface deformation measurement: historical developments, recent advances and future goals*, Measurement Science and Technology, **29**, 8, 82001, 2018.

13. W.H. PETERS, W.F. RANSON, *Digital imaging techniques in experimental stress analysis*, Optical Engineering, **21**, 3, 427–431, 1982.

14. A. CARTWRIGHT-TAYLOR, I.G. MAIN, I.B. BUTLER, F. FUSSEIS, M. FLYNN, A. KING, *Catastrophic failure: how and when? Insights from 4D in-situ x-ray micro-tomography*, Journal of Geophysical Research: Solid Earth, **125**, 8, e2020JB019642, 2020.

15. J.A. MCBECK, B. CORDONNIER, S. VINCIGUERRA, F. RENARD, *Volumetric and shear strain localization in mt. Etna basalt*, Geophysical Research Letters, **46**, 5, 2425–2433, 2019.

16. J.Z. Zhang, X.P. Zhou, *Fracture process zone (FPZ)in quasi-brittle materials: review and new insights from flawed granite subjected to uniaxial stress*, Engineering Fracture Mechanics, **274**, 108795, 2022.

17. C. Couture, P. Bésuelle, *A true triaxial experimental study on porous vosges sandstone: from strain localization precursors to failure using full-field measurements*, International Journal of Rock Mechanics and Mining Sciences, **153**, 105031, 2022.

18. B. Voight, *A method for prediction of volcanic eruptions*, Nature, **332**, 6160, 125–130, 1988.

19. B. Voight, *A relation to describe rate-dependent material failure*, Science, **243**, 4888, 200–203, 1989.

20. B. Voight, R.R. Cornelius, *Prospects for eruption prediction in near real-time*, Nature, **350**, 6320, 695–698, 1991.

21. A.F. Bell, M. Naylor, M.J. Heap, I.G. Main, *Forecasting volcanic eruptions and other material failure phenomena: an evaluation of the failure forecast method*, Geophysical Research Letters, **38**, 15, 2011.

22. S.W. Hao, H. Yang, D. Elsworth, *An accelerating precursor to predict "time-to-failure" in creep and volcanic eruptions*, Journal of Volcanology and Geothermal Research, **343**, 252–262, 2017.

23. A.F. Bell, C.R.I. Kilburn, *Precursors to dyke-fed eruptions at basaltic volcanoes: insights from patterns of volcano-tectonic seismicity at Kilauea volcano, Hawaii*, Bulletin of Volcanology, **74**, 2, 325–339, 2012.

24. R.R. Cornelius, P.A. Scott, *A material failure relation of accelerating creep as empirical description of damage accumulation*, Rock Mechanics and Rock Engineering, **26**, 3, 233–252, 1993.

25. R.R. Cornelius, B. Voight, *Seismological aspects of the 1989–1990 eruption at redoubt volcano, Alaska: the Materials Failure Forecast Method (FFM)with RSAM and SSAM seismic data*, Journal of Volcanology and Geothermal Research, **62**, 1, 469–498, 1994.

26. R.R. Cornelius, B. Voight, *Graphical and pc-software analysis of volcano eruption precursors according to the Materials Failure Forecast Method (FFM)*, Journal of Volcanology and Geothermal Research, **64**, 3, 295–320, 1995.

27. Y. Lavallée, P.G. Meredith, D.B. Dingwell, K.U. Hess, J. Wassermann, B. Cordonnier, A. Gerik, J.H. Kruhl, *Seismogenic lavas and explosive eruption forecasting*, Nature, **453**, 7194, 507–510, 2008.

28. Y. Niu, X.P. Zhou, *Forecast of time-of-instability in rocks under complex stress conditions using spatial precursory ae response rate*, International Journal of Rock Mechanics and Mining Sciences, **147**, 104908, 2021.

29. R. Smith, P.R. Sammonds, C.R.J. Kilburn, *Fracturing of volcanic systems: experimental insights into pre-eruptive conditions*, Earth and Planetary Science Letters, **280**, 1-4, 211–219, 2009.

30. J.Z. Zhang, X.P. Zhou, *Forecasting catastrophic rupture in brittle rocks using precursory ae time series*, Journal of Geophysical Research: Solid Earth, **125**, 8, 2020.

31. X.P. Zhou, C.Q. Li, *Prospective forecast of sliding instability time using a precursory ae time series*, Tribology International, **176**, 107887, 2022.

32. T. CARLÀ, E. INTRIERI, F. DI TRAGLIA, T. NOLESINI, G. GIGLI, N. CASAGLI, *Guidelines on the use of inverse velocity method as a tool for setting alarm thresholds and forecasting landslides and structure collapses*, Landslides, **14**, 2, 517–534, 2017.

33. X. FAN, Q. XU, J. LIU, S.S. SUBRAMANIAN, C. HE, X. ZHU, L. ZHOU, *Successful early warning and emergency response of a disastrous rockslide in Guizhou province, China*, Landslides, **16**, 12, 2445–2457, 2019.

34. C. KILBURN, D.N. PETLEY, *Forecasting giant, catastrophic slope collapse: lessons from vajont, Northern Italy*, Geomorphology, **54**, 21–32, 2003.

35. C.R.J. KILBURN, *Multiscale fracturing as a key to forecasting volcanic eruptions*, Journal of Volcanology and Geothermal Research, **125**, 3, 271–289, 2003.

36. R. SMITH, C.R.J. KILBURN, *Forecasting eruptions after long repose intervals from accelerating rates of rock fracture: June 1991 eruption of Mount Pinatubo, Philippines*, Journal of Volcanology and Geothermal Research, **191**, 1-2, 129–136, 2010.

37. R. SMITH, C.R.J. KILBURN, P.R. SAMMONDS, *Rock fracture as a precursor to lava dome eruptions at Mount st Helens from June 1980 to October 1986*, Bulletin of Volcanology, **69**, 6, 681–693, 2007.

38. J. CORCORAN, *Rate-based structural health monitoring using permanently installed sensors*, Proceedings of the Royal Society. A, Mathematical, Physical, and Engineering Sciences, **473**, 2205, 1–18, 2017.

39. R. HILL, J.W. HUTCHINSON, *Bifurcation phenomena in the plane tension test*, Journal of the Mechanics and Physics of Solids, **23**, 4, 239–264, 1975.

40. D.A. LOCKNER, J.D. BYERLEE, V.S. KUKSENKO, A.V. PONOMAREV, A. SIDORIN, *Quasi-static fault growth and shear fracture energy in granite*, Nature, **350**, 39–42, 1991.

41. A.P. RATHBUN, C. MARONE, *Effect of strain localization on frictional behavior of sheared granular materials*, Journal of Geophysical Research-Solid Earth, **115**, 2010.

42. R.E. RIZZO, D. HEALY, M.J. HEAP, N.J. FARRELL, *Detecting the onset of strain localization using two-dimensional wavelet analysis on sandstone deformed at different effective pressures*, Journal of Geophysical Research: Solid Earth, **123**, 12, 10460–10478, 2018.

43. J.W. RUDNICKI, J.R. RICE, *Conditions for the localization of deformation in pressure-sensitive dilatant materials*, Journal of the Mechanics and Physics of Solids, **23**, 6, 371–394, 1975.

44. H. ZHANG, G.Y. HUANG, H.P. SONG, Y.L. KANG, *Experimental characterization of strain localization in rock*, Geophysical Journal International, **194**, 3, 1554–1558, 2013.

45. G.D. NGUYEN, H.H. BUI, *A thermodynamics and mechanism-based framework for constitutive models with evolving thickness of localisation band*, International Journal of Solids and Structures, **187**, 100–120, 2020.

46. V. THAKUR, S. NORDAL, G. VIGGIANI, P. CHARRIER, *Shear bands in undrained plane strain compression of norwegian quick clays*, Canadian Geotechnical Journal, **55**, 1, 45–56, 2018.

47. N.G.W. COOK, *The failure of rock*, International Journal of Rock Mechanics and Mining Sciences and Geomechanics Abstracts, **2**, 4, 389–403, 1965.

48. B.G. Tarasov, T.R. Stacey, *Features of the energy balance and fragmentation mechanisms at spontaneous failure of Class I and Class II rocks*, Rock Mechanics and Rock Engineering, **50**, 10, 2563–2584, 2017.

49. Q.Z. Zhu, Q.J. Yu, *Theoretical analysis of the triggering condition of Class-ii rock behaviors*, International Journal of Rock Mechanics and Mining Sciences, **153**, 105109, 2022.

50. S.W. Hao, F. Rong, M.F. Lu, H.Y. Wang, M.F. Xia, F.J. Ke, Y.L. Bai, *Power-law singularity as a possible catastrophe warning observed in rock experiments*, International Journal of Rock Mechanics and Mining Sciences, **60**, 253–262, 2013.

51. L.H. Liang, X.N. Li, H.Y. Liu, Y.B. Wang, Y.G. Wei, *Power-law characteristics of damage and failure of ceramic coating systems under three-point bending*, Surface and Coatings Technology, **285**, 113–119, 2016.

52. J. Xue, S.W. Hao, J. Wang, F.J. Ke, C.S. Lu, Y.L. Bai, *The changeable power law singularity and its application to prediction of catastrophic rupture in uniaxial compressive tests of geomedia*, Journal of Geophysical Research: Solid Earth, **123**, 4, 2645–2657, 2018.

53. S. Jonsson, *Fault slip distribution of the 1999 M_w 7.1 Hector Mine, California, Earthquake, Estimated from Satellite Radar and GPS Measurements*, Bulletin of the Seismological Society of America, **92**, 4, 1377–1389, 2002.

54. J.R. Weiss, R.J. Walters, Y. Morishita, T.J. Wright, M. Lazecky, H. Wang, E. Hussain, A.J. Hooper, J.R. Elliott, C. Rollins, C. Yu, P.J. González, K. Spaans, Z. Li, B. Parsons, *High-resolution surface velocities and strain for anatolia from sentinel-1 InSAR and GNSS data*, Geophysical Research Letters, **47**, 17, 2020.

55. R. Bürgmann, P.A. Rosen, E.J. Fielding, *Synthetic aperture radar interferometry to measure earth's surface topography and its deformation*, Annual Review of Earth and Planetary Sciences, **28**, 1, 169–209, 2000.

56. H. Wang, T.J. Wright, J.Z. Liu, L.C. Peng, *Strain rate distribution in south-central Tibet from two decades of InSAR and GPS*, Geophysical Research Letters, **46**, 10, 5170–5179, 2019.

57. X.P. Zhou, J.Z. Zhang, *Damage progression and acoustic emission in brittle failure of granite and sandstone*, International Journal of Rock Mechanics and Mining Sciences, **143**, 104789, 2021.

58. K. Aki, *A new view of earthquake and volcano precursors*, Earth, Planets and Space, **56**, 8, 689–713, 2004.

59. C. Scholz, *Whatever happened to earthquake prediction*, Geotimes, **42**, 3, 16–19, 1997.

60. P.G. Silver, H. Wakita, *A search for earthquake precursors*, Science, **273**, 5271, 77–78, 1996.

61. S.J. Zhou, S.W. Hao, D. Elsworth, *Magnitude and variation of the critical power law exponent and its physical controls*, Physica A: Statistical Mechanics and Its Applications, **510,** 552–557, 2018.

Received July 23, 2023; revised version April 2, 2024.
Published online April 23, 2024.